

Enhanced energy coupling for indirectly driven inertial confinement fusion

Y. Ping^{1*}, V. A. Smalyuk¹, P. Amendt¹, R. Tommasini¹, J. E. Field¹, S. Khan¹, D. Bennett¹, E. Dewald¹, F. Graziani¹, S. Johnson¹, O. L. Landen¹, A. G. MacPhee¹, A. Nikroo¹, J. Pino¹, S. Prisbrey¹, J. Ralph¹, R. Seugling¹, D. Strozzi¹, R. E. Tipton¹, Y. M. Wang¹, E. Loomis², E. Merritt² and D. Montgomery²

Recent experiments in the study of inertial confinement fusion (ICF) at the National Ignition Facility (NIF) in the United States have reached the so-called alpha-heating regime^{1–3}, in which the self-heating by fusion products becomes dominant, with neutron yields now exceeding 1×10^{16} (ref. 4). However, there are still challenges on the path towards ignition, such as minimization of the drive asymmetry, suppression of laser-plasma instabilities, and mitigation of fabrication features⁵. In addition, in the current cylindrical-hohlraum indirect drive schemes for ICF, a strong limitation is the inefficient ($\leq 10\%$) absorption of the laser-produced hohlraum X-rays by the capsule as set by relative capsule-to-hohlraum surface areas. Here we report an experiment demonstrating ~30% energy coupling to an aluminium capsule in a rugby-shaped⁶, gold hohlraum. This high coupling efficiency can substantially increase the tolerance to residual imperfections and improve the prospects for ignition, both in mainline single-shell hot-spot designs and potential double-shell targets.

Reproducing the fusion power source for the Sun in a laboratory on the Earth has long been a cherished scientific goal due to its near limitless energy potential. Since the idea of using high-power lasers to create fusion conditions in the laboratory was first published in 1972⁷, much progress has been made to understand the inherent challenges, particularly the degrading effects of hydrodynamic instabilities and drive asymmetries. Successively larger lasers have been constructed over the past decades to drive ever larger targets that are predicted to be more robust to all sources of implosion degradation. The minimum laser energy required for ignition scales as $E_{\text{ign}} \sim \eta^{-1} \alpha^{1.8} v_{\text{imp}}^{-6} P_a^{-0.8}$ (refs 8,9), where η is the hohlraum-to-capsule coupling efficiency, α is in-flight adiabat parameter that measures the fuel entropy, v_{imp} is the peak implosion velocity of the shell and P_a is the peak ablation pressure. Much effort has focused on increasing v_{imp} and P_a while keeping a low fuel adiabat¹⁰. Relatively less attention has been paid towards improving η by increasing the capsule size because within the current laser drive capability a larger capsule will result in asymmetry if the standard cylindrical hohlraum geometry is followed. A substantial increase in η with rugby-shaped hohlraums will allow larger capsules to be driven while maintaining reasonable symmetry.

A typical energy partition in the standard indirect drive design is the following⁵: with ~2 MJ input laser energy, ~1.6 MJ is converted to X-rays in the hohlraum, ~150 kJ is absorbed by the capsule¹ and ~8–15 kJ is in the kinetic energy of the shell². It is clear that there is a tremendous energy loss in the coupling from the hohlraum to the capsule, so that enhancing this coupling efficiency is an effective way to improve performance in the indirect-drive ICF.

Efficient energy coupling would benefit both the mainline central-hot-spot (CHS) approach, where a hot spot initiates the thermonuclear burn, and a complementary scheme for volumetric ignition using double-shell (DS) capsules¹¹. In the latter, a high-Z inner shell is added to provide high inertial confinement and efficient radiation trapping. The DS approach generally provides less gain than CHS due to less fuel mass, yet it has potential benefits such as a low ignition threshold (4–5 keV versus 10–12 keV in CHS), relaxed requirements on symmetry, and non-cryogenic fielding^{11,12}. The ignition threshold is lower than the CHS approach because of the large reduction in radiation loss¹¹, which is one of the major energy losses in the hot spot². Elements of the DS concept have been successfully tested using low-Z inner shells at the OMEGA and NOVA laser facilities^{13–16}. In contrast to the single-shell approach, where the laser drive generates successively stronger shocks, the DS approach uses a shorter reverse-ramp pulse shape for impulsively driving the outer shell, thus minimizing the adverse effects of hohlraum plasma filling on late-time laser propagation¹⁷.

The NIF¹⁸ experiment for demonstrating high coupling used a large Al capsule in a Au rugby hohlraum driven at 1 MJ of laser energy with a reverse-ramp pulse shape as in the DS approach. A single-shell target was used in this experiment since it is sufficient for the study of the hohlraum-to-capsule coupling in a DS configuration. Typically ICF targets employ a low-Z capsule (Be, CH or high-density carbon (HDC)) mainly for a high ablation rate⁹. However, these materials are not sufficiently opaque to prevent preheat which raises the fuel entropy, thus a higher-Z dopant shielding layer is required. The pure Al ablator in our target differs from previous ablators fielded on the NIF by providing effective self-screening of preheat of the encapsulated DT fuel. The Al shell trajectory during the implosion was measured with streaked X-ray radiography to provide both the shell velocity and mass remaining. The mass remaining is in good agreement with an analytical estimate using the measured hohlraum radiation temperature and shell velocity as inputs to a rocket model. The shell kinetic energy was measured to be 34 ± 4 kJ with a ~1 MJ laser drive, which is two to four times that which was achieved in the recent record-yield shots with a ~2 MJ laser drive². Given that the typical rocket efficiency for an imploding Al ablator is ~10% (ref. 19), 34 kJ shell kinetic energy corresponds to >300 kJ coupled into the capsule, consistent with detailed comparison between simulated and measured quantities as described in this paper.

The experimental configuration uses a standard X-ray backlighting set-up, as illustrated in Fig. 1. The time history of the radiation temperature T_r , measured through the laser entrance hole using the Dante diagnostic (an absolutely calibrated X-ray diode array²⁰), is

¹Lawrence Livermore National Laboratory, Livermore, CA, USA. ²Los Alamos National Laboratory, Los Alamos, NM, USA. *e-mail: ping2@llnl.gov

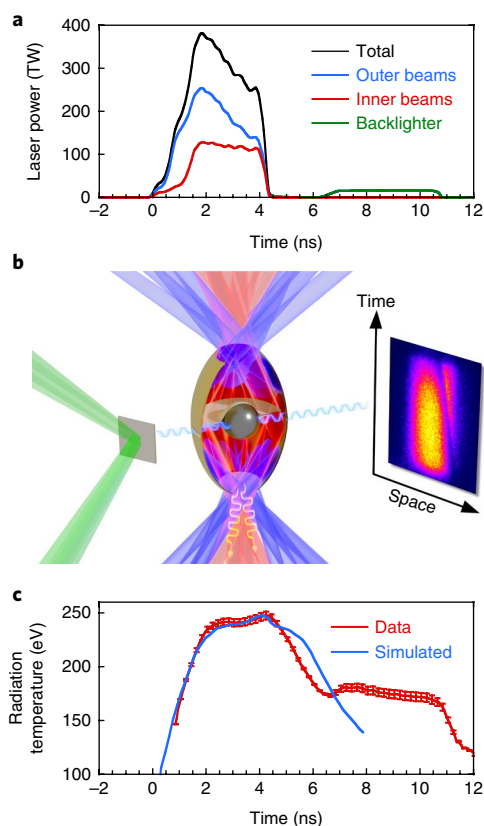


Fig. 1 | Experimental set-up and measured time history of laser power and radiation temperature. **a**, Laser power versus time for outer beams (blue), inner beams (red), total (black) and backlighter (green). The laser drive had a reverse-ramp shape with a duration of ~4 ns, a peak power of 350 TW and a total energy of 1.08 MJ, of which 68 kJ was used for the backlighter. **b**, Experimental schematic showing representative outer beams (blue) and inner beams (red). A Zr foil located at 12 mm from the target centre was irradiated by eight NIF beams to generate a 16 keV backlighter (green)²⁶. The hard X-rays are necessary to provide sufficient transmission through the imploded Al shell. Two opposing windows made of HDC were patched on the hohlraum wall along the radiography axis to allow X-rays to pass through. **c**, Measured and simulated radiation temperature versus time. The error bars are standard deviation among the four channels of Dante.

shown together with simulation results. The radiation temperature follows the fast rise of the driver pulse, reaching a plateau near the peak power and then decreasing as the drive laser turns off. The peak radiation temperature reaches 248 ± 3 eV. The bump at 7–11 ns is an artefact due to the backlighter. The simulated time history of T_r agrees well with the data while the laser is on, and decays more slowly than the data after the laser turns off. This difference turns out to be energetically insignificant, as the simulated and measured shell trajectories are in excellent agreement (as will be seen later in the 2D results).

The time-resolved one-dimensional (1D) radiograph²¹ of the Al shell recorded by an X-ray streak camera²² is shown in Fig. 2a. The radiograph shows a clear trajectory of a single limb over a relatively long recording time of 4.6 ns within a single shot. The implosion velocity is measured by tracking the position of the minimum of transmission, which is found to be $1.51 \pm 0.08 \times 10^7$ cm s⁻¹, as shown in Fig. 2b. The simulated velocity is in good agreement with the measurements either with asymmetric drive (blue solid line) or with symmetrized drive (blue dashed line). The difference in velocity from the simulations with and without drive asymmetry provides

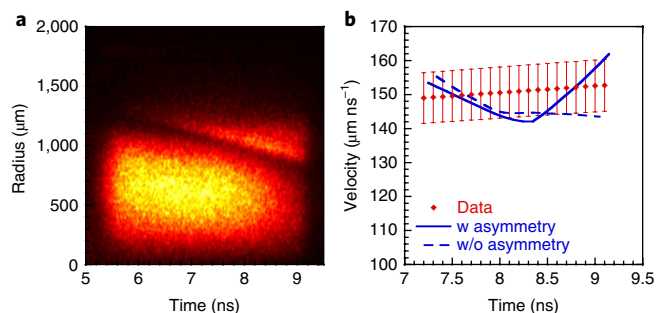


Fig. 2 | Results from 1D X-ray radiography. **a**, Streaked 1D X-ray radiograph. **b**, Measured and simulated shell velocity versus time. The velocity is calculated by taking linear derivatives of four sequential radius points. The error bars in velocity derive from the error bars in radius, which are statistical uncertainty in locating the radius of minimum transmission affected by noise.

a bound on the effect of asymmetry on the average shell velocity at the hohlraum midplane, which is still within the experimental errors. The simulations also confirm that the transmission minimum velocity is equal to the shell velocity or implosion velocity over this time window.

With the measured T_r and the shell velocity v_{imp} , the remaining shell mass can be estimated using a rocket model¹⁹:

$$v_{\text{imp}} \text{ (cm s}^{-1}\text{)} = 10^7 \sqrt{T_r \text{ (100 eV)}} \ln \left(\frac{m_0}{m} \right) / 1.25 \quad (1)$$

where T_r is in hundreds of eV or keV, m_0 is the initial mass and m is the mass remaining. The factor of 1.25 in equation (1) is due to the dependence on the ablator material, $v_{\text{imp}} \sim \sqrt{(1+Z)/A}$. The numerical formula in ref. ¹⁹ is based on simulations with a CH ablator (fully ionized, average $Z=3.5$, $A=6.5$). The implosion velocity is reduced by factor of 1.25 for the Al ablator (ionized to He-like, $Z=11$, $A=27$) relative to a CH ablator. Given the measured peak radiation temperature $T_r=2.48$ keV, $v_{\text{imp}}=1.51 \times 10^7$ cm s⁻¹ and $m_0=10.5$ mg, the mass remaining is estimated to be 3.2 mg. The shell kinetic energy then follows as $E = \frac{1}{2} m v_{\text{imp}}^2 \sim 36$ kJ.

From the lineout of the 1D radiograph the radial profile of the shell mass density can be reconstructed to obtain a more accurate measurement of the mass remaining. The shell density profile is reconstructed using a forward iterative inversion procedure²³. Figure 3 shows the reconstructed density profile at $t=8.4$ ns. By integrating this profile under the assumption of spherical symmetry and cold opacity, the mass remaining is found to be 3.0 ± 0.2 mg, in good agreement with the estimate from the rocket model. Figure 3 also shows the calculated transmission profile from the reconstructed density profile, giving good agreement with the data, and thus validating the reconstruction. Together with the measured shell velocity, the shell kinetic energy is found to be 34 ± 4 kJ.

We have also performed two-dimensional (2D) radiography²⁴ to evaluate the symmetry of the imploded Al shell. Due to the limited HDC diagnostic patch size, the 2D snapshots were taken at a later time than the 1D radiograph when the shell was smaller. Figure 4a shows a 2D radiograph taken at 10.5 ns. Although at this delay the capsule was still too large to provide a suitable lineout as in the 1D radiograph, the shape can be analysed for a symmetry assessment. The average radius of the transmission minimum is measured to be 550 ± 20 μm, and the second Legendre mode P_2 , which indicates whether the shape is prolate (positive) or oblate (negative)²⁵, is $+40$ μm, or ~7% of the radius. Simulations suggest that P_2 is smaller at earlier time. We can thus use this value to estimate an upper limit on the asphericity-induced uncertainty in the mass remaining and

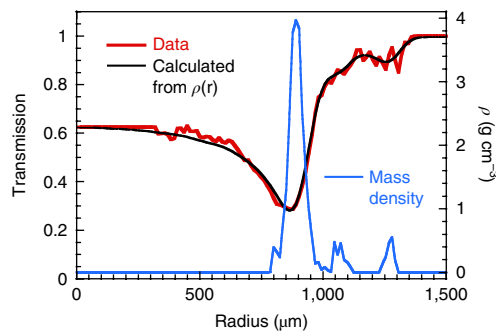


Fig. 3 | Comparison of the radiograph lineout at 8.4 ns (red) and calculated transmission profile (black) from the reconstructed density profile (blue).

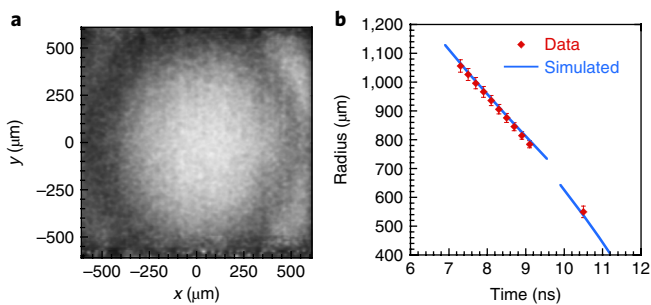


Fig. 4 | Results from 2D X-ray radiography. a, 2D X-ray radiograph at 10.5 ns. **b**, Comparison of measured and simulated shell radius versus time. The data at 7–9 ns are from the 1D radiography shot, and the data point at 10.5 ns is from the 2D snapshot. These two shots had different HDC patch sizes. The error bars in radius are statistical and originate from locating the radius of minimum transmission in a radiograph affected by noise.

the shell kinetic energy measured at 8.4 ns. The radius at the pole would be $1.5 \times P_2 \sim 60 \mu\text{m}$ larger, or the average velocity 11% lower. From the rocket model the corresponding mass remaining would be 12% larger. Overall the kinetic energy is $\propto mv^2 \sim 10\%$ less, which is within the experimental error.

The measured radius versus time from both the 1D radiograph at 7–9 ns and the 2D snapshot at 10.5 ns is plotted in Fig. 4b. The simulated time history of the radius, taking into account the different HDC patch sizes for these two shots, shows good agreement with the data. Table 1 presents a list of measured quantities in comparison with simulated results, indicating good agreement between the simulations and experimental data. It should be noted that high convergence is not required for the DS approach: the outer shell needs to converge by only a factor of $\sim 5\times$ even in the full-scale ignition design.

The energy coupling is mainly enhanced by a combination of the large capsule-to-hohlraum ratio and the short drive duration. In the indirect drive scheme, the hohlraum is filled with X-rays and the coupling to the capsule depends mainly on a geometric effect: the surface area ratio of the capsule to the hohlraum. Our capsule is 50% larger in radius than the standard single-shell capsule, leading to a higher coupling efficiency. The typical pulse shape in recent record-yield shots has a few small peaks followed by a main peak starting around 10 ns (ref. ³). Therefore the capsule is already partially compressed at the start of the main drive for these schemes, further reducing the area ratio and energy coupling to the capsule. The pulse shape used in our experiment is a short reverse ramp with high power early in time when the capsule is still large, enabling

Table 1 | Comparison of measured and simulated quantities

Quantity	Measured	Simulated
Peak T_e (eV)	248 ± 3	248
$\langle R \rangle$ (μm) at 8.4 ns	890 ± 20	884
v_{imp} ($\mu\text{m ns}^{-1}$) at 8.4 ns	151 ± 8	144
Mass (mg) at 8.4 ns	3.0 ± 0.2	3.67
Shell kinetic energy (kJ) at 8.4 ns	34 ± 4	38
Shell FWHM (μm) at 8.4 ns	89 ± 14	100
$\langle R \rangle$ (μm) at 10.5 ns	550 ± 20	538

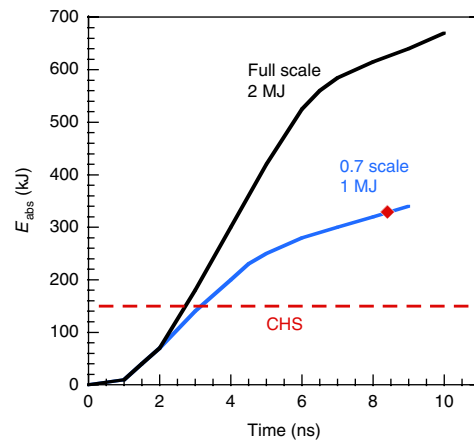


Fig. 5 | Energy coupled to the capsule as a function of time from 0.7 \times subscale and full-scale simulations. The energy absorbed at the experimental probe time 8.4 ns is 330 kJ, marked as the red dot in the 0.7 \times curve. The typical absorbed energy 150 kJ in standard CHS full-scale design is marked as red dashed line for comparison.

higher coupling efficiency. Furthermore, the rugby shape of the hohlraum helps minimize surface area losses compared with cylindrical hohlraums, which is the dominant energy loss mechanism in hohlraums. Since the efficiency is enhanced mainly by the geometry and the short drive duration, the high coupling will not be significantly decreased by the presence of fill tube or mix at inner layers.

The time history of the absorbed energy by the capsule from simulations is plotted in Fig. 5 for this 0.7 \times subscale campaign with 1 MJ drive (blue line). The $\sim 30\%$ coupling efficiency at 8.4 ns is more than three times greater than the current CHS designs for indirect drive. Although the pulse shape is unique to the DS approach, a novel hohlraum shape accommodating a larger capsule could markedly enhance the coupling efficiency in the CHS approach as well. In the next phase of our experiments, the Al capsule will be filled with DT gas to enable nuclear diagnostics; shape-tuning campaigns will aim to improve the symmetry; and an additional factor of two increase of total coupled energy up to ~ 700 kJ is projected for a full-scale design (see Methods) and 2 MJ drive, as shown in Fig. 5 (black line).

Online content

Any methods, additional references, Nature Research reporting summaries, source data, statements of data availability and associated accession codes are available at <https://doi.org/10.1038/s41567-018-0331-5>.

Received: 8 February 2018; Accepted: 26 September 2018;
Published online: 29 October 2018

References

- Hurricane, O. A. et al. Fuel gain exceeding unity in an inertially confined fusion implosion. *Nature* **506**, 343–348 (2014).
- Hurricane, O. A. et al. Inertially confined fusion plasmas dominated by alpha-particle self-heating. *Nat. Phys.* **12**, 800–806 (2016).
- Doeppner, T. et al. Demonstration of high performance in layered deuterium-tritium capsule implosions in uranium hohlraums at the National Ignition Facility. *Phys. Rev. Lett.* **115**, 055001 (2015).
- Le Pape, S. et al. Fusion energy output greater than the kinetic energy of an imploding shell at the National Ignition Facility. *Phys. Rev. Lett.* **120**, 245003 (2018).
- Betti, R. & Hurricane, O. A. Inertial-confinement fusion with lasers. *Nat. Phys.* **12**, 435–448 (2016).
- Amendt, P. A. et al. Rugby-like hohlraum experimental designs for demonstrating X-ray drive enhancement. *Phys. Plasmas* **15**, 012702 (2008).
- Nuckolls, J., Wood, L., Thiessen, A. & Zimmerman, G. Laser compression of matter to super-high densities: thermonuclear (CTR) applications. *Nature* **239**, 139–142 (1972).
- Herrmann, M. C., Tabak, M. & Lindl, J. Ignition scaling laws and their application to capsule design. *Phys. Plasmas* **8**, 2296–2304 (2001).
- Atzeni, S. & Meyer-ter-vehn, J. *The Physics of Inertial Fusion* (Oxford Univ. Press, New York, 2004).
- Lindl, J. et al. Review of the National Ignition Campaign 2009–2012. *Phys. Plasmas* **21**, 020501 (2014).
- Amendt, P. A. et al. Assessing the prospects for achieving double-shell ignition on the National Ignition Facility using vacuum hohlraums. *Phys. Plasmas* **14**, 056312 (2007).
- Kline, J. L. et al. Developing one-dimensional implosions for inertial confinement science. *High Power Laser Sci. Eng.* **4**, 44–50 (2016).
- Amendt, P. A. et al. Hohlraum-driven ignitionlike double-shell implosions on the OMEGA laser facility. *Phys. Rev. Lett.* **94**, 065004 (2005).
- Robey, H. F. et al. Hohlraum-driven mid-Z (SiO₂) double-shell implosions on the OMEGA laser facility and their scaling to NIF. *Phys. Rev. Lett.* **103**, 145003 (2009).
- Varnum, W. S. et al. Progress toward ignition with noncryogenic double-shell capsules. *Phys. Rev. Lett.* **84**, 5153–5155 (2000).
- Kyrala, G. A. et al. Detailed diagnosis of a double-shell collision under realistic implosion conditions. *Phys. Plasmas* **13**, 056306 (2006).
- Callahan, D. A. et al. Exploring the limits of case-to-capsule ratio, pulse length, and picket energy for symmetric hohlraum drive on the National Ignition Facility laser. *Phys. Plasmas* **25**, 056305 (2018).
- Miller, G. H., Moses, E. I. & Wuest, C. R. The National Ignition Facility. *Opt. Eng.* **43**, 2841–2853 (2004).
- Lindl, J. Development of the indirect-drive approach to inertial confinement fusion and the target physics basis for ignition and gain. *Phys. Plasmas* **2**, 3933–4024 (1995).
- Dewald, E. L. et al. Dante soft X-ray power diagnostic for National Ignition Facility. *Rev. Sci. Instrum.* **75**, 3759–3761 (2004).
- Hicks, D. G. et al. Streaked radiography measurements of convergent ablator performance. *Rev. Sci. Instrum.* **81**, 10E304 (2010).
- Opachich, Y. P. et al. X-ray streak camera cathode development and timing accuracy of the 4 ω ultraviolet fiducial system at the National Ignition Facility. *Rev. Sci. Instrum.* **83**, 10E123 (2012).
- Tommasini, R. et al. Tent-induced perturbations on areal density of implosions at the National Ignition Facility. *Phys. Plasmas* **22**, 056315 (2015).
- Rygg, J. R. et al. 2D X-ray radiography of imploding capsules at the National Ignition Facility. *Phys. Rev. Lett.* **112**, 195001 (2014).
- Glenn, S. M. et al. Extracting core shape from X-ray images at the National Ignition Facility. *Rev. Sci. Instrum.* **83**, 10E519 (2012).
- Barrios, M. A. et al. X-ray area backlighter development at the National Ignition Facility. *Rev. Sci. Instrum.* **85**, 11D502 (2014).

Acknowledgements

We thank the NIF team at LLNL for excellent laser operation and technical support. We also would like to thank the target fabrication group for outstanding work on development and delivery of the high-quality Al capsules. This work was performed under the auspices of the US DOE by LLNL under contract number DEAC52-07NA27344. Y.P. acknowledges support from the DOE/ECRP Program. Y.M.W. acknowledges LLNL LDRD (17-ERD-048) support.

Author contributions

Y.P. and V.A.S. carried out the experimental set-up and execution with help from R.T., E.D., A.G.M. and J.E.R. P.A. was the target designer and performed the pre- and post-shot simulations. R.T., J.F., S.K., Y.P., V.A.S. and O.L.L. contributed to the data analysis. D.B., S.J., A.N., R.S. and Y.M.W. contributed to fabrication of the high-quality Al capsules. D.S. contributed to backscatter mitigation, F.G., J.P., S.P. and R.E.T. contributed to the planning and simulations. E.L., E.M. and D.M. contributed to the backlighter and radiography development. Y.P. wrote the manuscript and P.A. wrote the simulation and full design sections. Y.P., V.A.S., P.A., R.T., O.L.L., A.G.M. and Y.M.W. contributed to the manuscript improvements.

Competing interests

The authors declare no competing interests.

Additional information

Supplementary information is available for this paper at <https://doi.org/10.1038/s41567-018-0331-5>.

Reprints and permissions information is available at www.nature.com/reprints.

Correspondence and requests for materials should be addressed to Y.P.

Publisher's note: Springer Nature remains neutral with regard to jurisdictional claims in published maps and institutional affiliations.

© The Author(s), under exclusive licence to Springer Nature Limited 2018

Methods

The Au rugby hohlraum was 9.86 mm long and 7.0 mm in diameter in the equatorial plane, with a laser entrance hole (LEH) diameter of 3.6 mm. The gas fill was pure ^4He at 0.3 mg cm^{-3} to help control time-dependent hohlraum drive asymmetry. The Al capsule supported by two 45 nm membranes was 3.0 mm in outer diameter and 148 μm thick, which is $\sim 50\%$ greater than typical ICF capsules that are $\sim 2 \text{ mm}$ in diameter. The detector was a streak camera with a slit for time-resolved 1D radiography with a magnification of 7.8 \times , and a framing camera with a pinhole array for a 2D snapshot with a magnification of 4.5 \times .

A 0.3-ns 30-TW laser pedestal was added at the beginning of the pulse to reduce laser backscatter. The backlighter was turned on from 5 ns to 9 ns for the 1D streaked radiography and from 7 ns to 11 ns for the 2D radiography. The total backscattered energy was estimated as 3.9% of the incident laser energy.

The simulations used to design and model the experiment are fully integrated (hohlraum + capsule + gas fill + laser), 2D radiation-hydrodynamic simulations based on the LASNEX code²⁷. The Au hohlraum and Al capsule are modelled using DCA opacities²⁸ and an electron thermal flux limiter of 0.03 (ref. ²⁹). This model reproduces the data without the need for ad hoc drive multipliers to account for 'missing energy', in contrast to standard hohlraum modelling³⁰. The simulations are post-processed with ray tracing to generate synthetic radiography images for comparison with the data. Inclusion of the HDC patches in the simulations is important, as the simulated peak Dante radiation temperature would otherwise be $\sim 7 \text{ eV}$ higher than the data, or $\sim 11\%$ higher in peak X-ray flux.

The shell opacity \times density ($\kappa\rho$) product is calculated from the 1D radiograph using a forward iterative unfolding procedure²³ that includes the spatial blurring introduced by the imaging slit and the temporal blurring and point spread function introduced by the streak camera. The density radial profile is directly calculated from the $\kappa\rho$ product to obtain a more accurate measurement of the mass remaining under the assumption that within the unablated region of the Al shell the approximation of cold opacity is valid at the photon energies used in our experiment. This assumption has been validated by simulations showing that the temperatures in the unablated region of the shell stay well below 60 eV. At 60 eV, we expect from the Boltzmann distribution that the Al K shell remains filled, which contributes 90% of cold opacity, and the L shell is only partially ionized, giving 95% of cold opacity. The temperature in the densest part of the unablated Al is about 20–25 eV at 9–12 ns from the simulations, so that the opacity difference is less than 5% from the cold values. We have also compared simulations using the cold opacity or the DCA model, and found the difference is less than 3%.

An envisaged ignition design is shown in Supplementary Fig. 1 for the capsule and in Supplementary Fig. 2 for the hohlraum, with the driver pulse shape shown in Supplementary Fig. 3. In this full-scale design, an Al outer shell of 3.6 mm diameter absorbs the hohlraum-generated X-rays to reach a peak speed of $>200 \mu\text{m ns}^{-1}$ before colliding with an inner shell of gold that is concentrically

suspended by a low-density ($<60 \text{ mg cm}^{-3}$), low-Z, inter-shell annular foam. This inner shell of nearly 300 μm radius encapsulates a liquid deuterium–tritium (D–T) fuel that is compressed by a factor of nearly 1000 \times to $\sim 200 \text{ g cm}^{-3}$ from the decelerating inner shell after reaching a peak velocity of $\sim 300 \mu\text{m ns}^{-1}$. The high-Z inner shell provides the required inertia to confine the fuel for tens of picoseconds while the fuel attains thermonuclear conditions: areal density of $\sim 0.3 \text{ g cm}^{-2}$ and threshold ignition temperature of $\sim 4 \text{ keV}$. This threshold ignition temperature is considerably lower than the nearly 12 keV required for the mainline cryogenic single-shell design, due to the high albedo of the inner shell to X-ray generation from the self-heated fuel. The main heating mechanism is from stopping of alpha particles (^4He) generated within the fuel, leading to peak D and T ion temperatures of 50–100 keV. The simulated thermonuclear energy yield of this double-shell design is $\sim 1 \times 10^{18}$, according to 2D radiation-hydrodynamic simulations.

The main challenges with achieving double-shell ignition are: achieving sufficiently high outer-shell implosion symmetry; obtaining an adequate hohlraum temperature to drive the outer shell to greater than $200 \mu\text{m ns}^{-1}$; ensuring benign levels of X-ray preheat symmetry on the inner shell; and tolerating the degrading effects of hydrodynamic instability growth on both the inner and outer surfaces of the inner shell to maintain shell integrity and to limit the degrading effects of mixing of inner-shell material with DT fuel. The subscale outer-shell experimental results reported here are intended to understand and control the drive and symmetry of the outer shell in preparation for eventual fielding of an interior (inner) shell. This ignition design is expected to provide a pathway to higher-gain double-shell targets that could provide the basis for a fusion–fission hybrid power plant³¹.

Data availability

The data that support the findings of this study are available from the corresponding author upon reasonable request.

References

- Zimmerman, G. B. & Kruer, W. L. Numerical simulation of laser-initiated fusion. *Comments Plasma Phys. Controlled Fusion* **2**, 51–60 (1975).
- Scott, H. A. & Hansen, S. B. Advances in NLTE modeling for integrated simulations. *High Energy Density Phys.* **6**, 39–47 (2010).
- Jones, O. S. et al. Progress towards a more predictive model for hohlraum radiation drive and symmetry. *Phys. Plasmas* **24**, 056312 (2017).
- Moody, J. et al. Progress in hohlraum physics for the National Ignition Facility. *Phys. Plasmas* **21**, 056317 (2014).
- Amendt, P., Milovich, J., Perkins, L.J. & Robey, H. An indirect-drive non-cryogenic double-shell path to 1ω Nd-laser hybrid inertial fusion–fission energy. *Nucl. Fusion* **50**, 105006 (2010).

Nature Research, brought to you courtesy of Springer Nature Limited (“Nature Research”)

Terms and Conditions

Nature Research supports a reasonable amount of sharing of content by authors, subscribers and authorised or authenticated users (“Users”), for small-scale personal, non-commercial use provided that you respect and maintain all copyright, trade and service marks and other proprietary notices. By accessing, viewing or using the nature content you agree to these terms of use (“Terms”). For these purposes, Nature Research considers academic use (by researchers and students) to be non-commercial.

These Terms are supplementary and will apply in addition to any applicable website terms and conditions, a relevant site licence or a personal subscription. These Terms will prevail over any conflict or ambiguity with regards to the terms, a site licence or a personal subscription (to the extent of the conflict or ambiguity only). By sharing, or receiving the content from a shared source, Users agree to be bound by these Terms.

We collect and use personal data to provide access to the nature content. ResearchGate may also use these personal data internally within ResearchGate and share it with Nature Research, in an anonymised way, for purposes of tracking, analysis and reporting. Nature Research will not otherwise disclose your personal data unless we have your permission as detailed in the Privacy Policy.

Users and the recipients of the nature content may not:

1. use the nature content for the purpose of providing other users with access to content on a regular or large scale basis or as a means to circumvent access control;
2. use the nature content where to do so would be considered a criminal or statutory offence in any jurisdiction, or gives rise to civil liability, or is otherwise unlawful;
3. falsely or misleadingly imply or suggest endorsement, approval, sponsorship, or association unless explicitly agreed to by either Nature Research or ResearchGate in writing;
4. use bots or other automated methods to access the nature content or redirect messages; or
5. override any security feature or exclusionary protocol.

These terms of use are reviewed regularly and may be amended at any time. We are not obligated to publish any information or content and may remove it or features or functionality at our sole discretion, at any time with or without notice. We may revoke this licence to you at any time and remove access to any copies of the shared content which have been saved.

Sharing of the nature content may not be done in order to create substitute for our own products or services or a systematic database of our content. Furthermore, we do not allow the creation of a product or service that creates revenue, royalties, rent or income from our content or its inclusion as part of a paid for service or for other commercial gain. Nature content cannot be used for inter-library loans and librarians may not upload nature content on a large scale into their, or any other, institutional repository.

To the fullest extent permitted by law Nature Research makes no warranties, representations or guarantees to Users, either express or implied with respect to the nature content and all parties disclaim and waive any implied warranties or warranties imposed by law, including merchantability or fitness for any particular purpose.

Please note that these rights do not automatically extend to content, data or other material published by Nature Research that we license from third parties.

If you intend to distribute our content to a wider audience on a regular basis or in any other manner not expressly permitted by these Terms please contact us at

onlineservice@springernature.com

The Nature trademark is a registered trademark of Springer Nature Limited.